GPR-assisted evaluation of probabilistic fatigue crack growth in rib-to-deck joints in orthotropic steel decks considering mixed failure models

Heng, Junlin; Zhou, Zhixiang; Zou, Yang ; Kaewunruen, Sakdirat

DOI
10.1016/j.engstruct.2021.113688

Publication date
2022

Document Version
Final published version

Published in
Engineering Structures

Engineering Structures 252 (2022) 113688

Contents lists available at ScienceDirect

Engineering Structures

journal homepage: www.elsevier.com/locate/engstruct

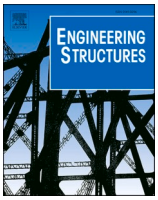

GPR-assisted evaluation of probabilistic fatigue crack growth in rib-to-deck joints in orthotropic steel decks considering mixed failure models

Junlin Heng [a,b], Zhixiang Zhou [a,*], Yang Zou [c], Sakdirat Kaewunruen [d]

[a] Department of Civil Engineering, College of Civil and Transportation Engineering, Shenzhen University, Shenzhen 518060, China
[b] Department of Engineering Structures, School of Civil Engineering and Geosciences, Delft University of Technology, Delft 2628 CN, the Netherlands
[c] Department of Bridge Engineering, School of Civil Engineering, Chongqing Jiaotong University, Chongqing 400074, China
[d] Department of Civil Engineering, School of Engineering, University of Birmingham, Birmingham B152TT, United Kingdom

ARTICLE INFO

Keywords:
Orthotropic steel deck
Rib-to-deck joint
Mixed failure models
Probabilistic fatigue crack growth
Gaussian process regression

ABSTRACT

Rib-to-deck (RD) welded joints in orthotropic steel decks (OSDs) of bridges demonstrates two major fatigue failure models, including the toe-to-deck (TTD) cracking and root-to-deck (RTD) cracking. Generally, the sole failure model is employed in the fatigue assessment of RD joints, causing a hot dispute on the dominant failure model. In this paper, the fatigue crack growth (FCG) in RD joints has been evaluated considering uncertainties and mixed failure models. A probabilistic fatigue crack growth (PFCG) model is at first established for the RD joint, in which two crack-like initial flaws are assumed at the weld toe and root of the RD joint. After that, the gaussian process regression is used to assist and boost the PFCG simulation. Then, the PFCG model is implemented on a typical OSD with the random traffic model. Finally, the result of the PFCG model is discussed in detail, including the failure model, fatigue reliability and life prediction, and crack size evolution. It is revealed that both the TTD and RTD cracking models have a notable contribution to fatigue failure and could not be ignored. More crucial, a remarkable reduction can be observed in the fatigue reliability of RD joints when considering mixed failure models. This study not only highlights the influence of mixed failure models on the fatigue performance of welded joints, but also provide an insight into the application of novel machine learning tools in solving the traditional structural issue.

1. Introduction

1.1. Research problem

1.1.1. Mixed failure models in RD joints

The orthotropic steel deck (OSD) [1] is a highly integral deck system fabricated with various types of welded connections. Among all the connections, the rib-to-deck (RD) welded joint accounts for the largest proportion, e.g., 50 times the bridge length of the RD joint can be observed in a typical OSD [2]. Moreover, the RD joint is directly influenced by the cyclic vehicle loads, as shown in Fig. 1. As a result, the RD joint becomes very prone to fatigue cracking after the bridge has been exploited for several decades [3], which hinders the further application of OSDs even if they illustrate superior performance and capacity over other deck systems.

In the RD joint, the weld toe and weld root are two critical sites for fatigue cracking due to the notable welding residual stress and discontinuity in geometry and material [4]. Accordingly, two different patterns of fatigue failure are observed in RD joints, including the toe-to-deck (TTD) crack and the root-to-deck (RTD) crack, as depicted in Fig. 1. Both the TTD crack and RTD crack are detrimental to the serviceability and durability of OSDs, which is of particular concern in the fatigue design.

1.1.2. Uncertainties in fatigue crack growth

As generally acknowledged, the fatigue crack growth (FCG) of welded connections is affected by a list of complicated factors with notable uncertainties [5]. To this end, the FCG process in RD joints becomes highly stochastic, which incurs difficulties in fatigue assessment. Besides, the uncertainty also results in the variation in the fatigue failure pattern in the RD joint, i.e., both the TTD cracking and RTD cracking were reported in the fatigue test and field inspection of OSDs [6]. To this end, a hot issue is still open to discussion over the fatigue cracking pattern of RD joints.

* Corresponding author at: College of Civil & Transportation Engineering, Shenzhen University, Shenzhen, China.
E-mail addresses: j.heng@szu.edu.cn (J. Heng), zhixiangzhou@szu.edu.cn (Z. Zhou).

https://doi.org/10.1016/j.engstruct.2021.113688
Received 30 May 2021; Received in revised form 27 November 2021; Accepted 28 November 2021
Available online 15 December 2021

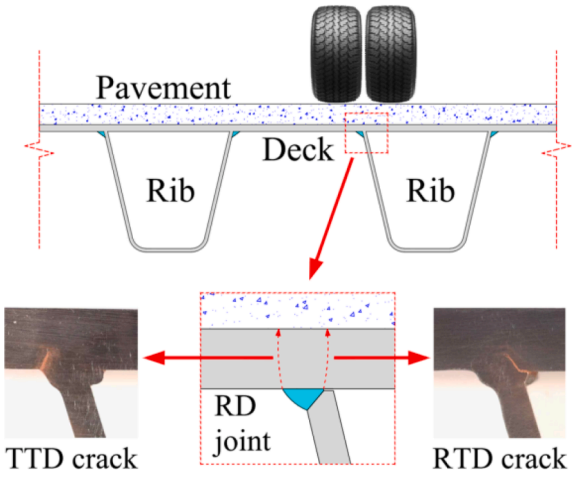

Fig. 1. Typical failure model of rib-to-deck joints.

1.2. State-of-the-art review

1.2.1. TTD or RTD cracking

The TTD cracking (as shown in Fig. 1) is commonly observed in the model fatigue test using the full-scale RD specimen [7], consisting of a deck plate and a closed U-ribs connected by two RD joints. Tian et al. [8] conducted the fatigue test of 7 RD specimens fabricated by partial joint penetration (PJP) welding. The TTD cracking was observed in 6 of 7 specimens, while only one shows the root-to-throat cracking. Heng et al. [9] carried out a similar fatigue test of 7 full-scale RD specimens, in which the TTD cracking was found in all the specimens. The test also suggests that the fatigue crack initiates at the deck toe and then grows in both the length and thickness direction of the deck until the failure. In the further study by Heng et al. [10], 4 more specimens were tested with the special effort to monitor the crack growth. Besides the same observation of the TTD cracking, the monitoring result suggests the semi-elliptical crack shape during the propagation. Similar tests were performed on RD specimens by Cheng et al. [11], Nagy et al.[12] and Li et al. [13], which also suggests a dominance of the TTD cracking. It is worth noting that a systematic fatigue test panel of RD joints was performed by Ocel et al. [14], with a total of 185 RD specimens. Except for the 30 runouts, the remain 155 specimens shows a remarkably high proportion of the TTD cracking, i.e., 125 specimens with the TTD cracking (about 81%). Among the 30 specimens without the TTD cracking, 16 specimens were fabricated with a large root gap deliberately, leading to the RTD cracking.

As aforementioned, the RTD cracking is another primary failure model of RD joint, especially when using the partial joint specimen [15]. Ya et al. [16] employed the rotational vibrator to test the partial joint specimen, consisting of a deck plate and a truncated rib wall. The RTD cracking was observed in all the 20 specimens with notable length, while only one mild TTD crack (95 mm-long) was found accompanied by a larger RTD crack (250 mm-long). Lv and Li [17] performed a similar fatigue test using the hydraulic loading machine, which also suggests the RTD cracking in all 9 specimens. In addition, Fu et al. [18] tested 40 similar partial joint specimens, with the RTD cracking observed in all the specimens.

Besides the pure TTD or RTD cracking, the two failure models were also simultaneously observed in the full-scale OSD specimens. Sim et al. [19] tested 6 full-scale OSD specimens of 10000 mm-long and 3000 mm-wide, which consists of 4 U-ribs and 3 floor beams. Three types of welding were used, including the 80% PJP, weld melt through (WMT), and the one alternating between 80% PJP and WMT every 1000 mm. A total of 7 cracks were observed in the 3 cracked specimens, 6 of which shown the TTD cracking. The only RTD crack initiated from the transition between the 80% PJP and WMT. According to the result, the RD joint is prone to TTD cracking when the penetration rate is properly controlled. Kainuma et al. [20] carried out the fatigue test on 12 full-scale OSD specimens of 2000 mm-long and 1400 mm-wide. The 9 cracked specimens shown a dominance of RTD cracking, i.e., 6 with the RTD and 3 with the TTD.

1.2.2. Preliminary consideration of mixed failure models

As discussed above, the fatigue performance of the RD joint is influenced by mixed failure models, including the TTD cracking and RTD cracking. Conner et al. [2] suggested that the RTD cracking leads to a fatigue resistance poorer than the TTD cracking. However, the RTD cracking could be effectively prevented by the proper penetration rate (i.e., between 70% and 95% with a target of 80%) and tight fit-up gap (i.e., less than0.5 mm) between the deck and U-rib. To this end, more attention and effort should be paid to the TTD cracking when the welding is implemented with reasonable configuration and procedures.

Wang et al. [21] investigated the FCG behaviour of RD joint using the extended finite element method (XFEM). Two initial flaws in the same size were assumed at the deck toe and root, and the numerical result shows the comparable behaviour of the TTD and RTD cracking models. Li et al. [22] proposed the concept of governing failure model, i.e., the fatigue failure of the RD joint is only governed by the failure model with the poorest performance. Based on this notion, the equivalent structural stress is solved under various failure models and compared to determine the governing failure model and the corresponding fatigue life. Luo et al. [23] proposed a similar approach using the governing fatigue model, in which the strain energy density is used as the evaluation indicator instead of the stress.

1.2.3. Advance in fatigue assessment

In most of the code of practices[242526], the fatigue assessment of the welded connection is made by checking the solved stress range and the number of cycles against the stress-life (S-N) curve, which is derived from the sufficient fatigue test data at the detail- or structural-level. The above S-N approach is simplified and practical but lacks transferability between different welded connections [2728]. Alternatively, the fracture mechanics [29] is employed to simulate the FCG in the welded connections, which can assess different details using the material test data only [30].

The FCG process involves prominent uncertainties, including the aleatory uncertainty in its nature and the epistemic uncertainty in modelling the issue [31]. As a solution, the deterministic fatigue assessment could be conducted based on the statistics of model parameters. For instance, the design S-N curve is usually established under the survival rate of 97.7%, i.e., the mean minus two times standard deviation [32]. Meanwhile, the vehicle effect is often represented by a standard fatigue truck, which is derived from the field survey and statistics [33]. The above statistics-based approach may be conservative but cannot fully reflect the random nature of fatigue [34]. Alternatively, the direct probabilistic approach is used, including the stress-based probabilistic stress-life (PSN) approach [3536] and fracture mechanics-based probabilistic fatigue crack growth (PFCG) method [3738]. The PSN approach modelled the fatigue strength and vehicle configuration as random variables [39], and the result is present in the form of the probabilistic distribution or reliability index [40].

The PFCG method is much more complicated than the PSN but can provide an in-depth insight into the hidden mechanism of fatigue cracking. Maljaar and Vrouwenvelder [41] established a PFCG model of rib-to-floor beam joint using the semi-elliptical crack model with 2 degree-of-freedoms (DOFs), and the model is executed with the analytical solution of stress intensity factors (SIFs). Heng et al. [10] proposed a similar PFCG model to derive PSN curve of RD joints considering the TTD cracking only. Likewise, Maljaar et al. [42] used the PFCG model to derive the PSN of RD joints respecting the RTD cracking. Wang [43] carried out the PFCG analysis to investigate the macro-crack initiation life (MCIL) of RD joints, which is the pre-detectable life of the crack

when its depth is less than 0.5 mm. A list of 2D XFEM-based deterministic analysis was carried out to solve the SIFs for the crack sizing from 0.1 to 0.5 mm. Then, the MCIL was solved through Monte Carlo simulations (MCS) with the linear interpolation of the solved SIFs.

1.3. Existing research gaps

As discussed above, the RD joint is prone to mixed failure models, including the TTD and RTD cracking. The issue caused special concerns and was addressed in several pioneered works. However, the reviewed studies mainly focused on the deterministic comparison of fatigue performance under different failure models. As a result, the fatigue behaviour is solely determined after the failure model with the poorest performance, i.e., the governing model. Nevertheless, the non-governing failure model still has the possibility to replace the governing model and cause failure due to the prominent uncertainty in fatigue. To this end, a probabilistic investigation is urgently required on the FCG behaviour of RD joints by considering the effect of mixed models.

Meanwhile, the state-of-the-art PFCG study generally employed the analytical solution or interpolation of deterministic finite element (FE) results. Although the high solution cost in the PFCG simulation can be mitigated in this way, the flexibility and accuracy of FE-based fracture analysis are not fully utilised. To this end, a novel approach is still lacked to fully integrate the FE analysis into the PFCG simulation, by which a delicate balance could be achieved between accuracy, efficiency, and flexibility.

1.4. Aim and structure of the paper

This study aims at the probabilistic evaluation of fatigue crack growth in rib-to-deck (RD) joints of orthotropic steel decks (OSDs), considering mixed failure models. The paper is organised as the followings: in Part 2, a probabilistic fatigue crack growth (PFCG) model is established for the RD joint, assuming two crack-like initial flaws at both the weld toe and root; in Part 3, a measurement-based random traffic model is employed to derive the vehicle-induced stress spectra at the RD joint in a selected prototype bridge; in Part 4, a gaussian process regression (GPR) model is trained to surrogate the finite element (FE)-based fracture analysis, through which the solution efficiency is notably improved with satisfying accuracy; in Part 5, the results from the above studies are discussed in detail, including the fatigue failure model, fatigue reliability and life prediction, crack size evolution, and remain fatigue life; in Part 6, the key conclusions are drawn based on the above investigation. The research not only highlights the influence of mixed failure models on the fatigue performance of RD joints in OSDs, but also provides an insight into the application of novel machine learning tools in solving the traditional structural issue.

2. Probabilistic fatigue crack growth model

2.1. Fatigue crack growth model

According to the above review and discussion, the crack model of RD joints is assumed with dual crack-like initial flaws at the weld toe and root, as shown Fig. 2. During the crack growth, the two cracks are assumed to stay in the perfect semi-elliptical shape with the aspect ratio varied with cycles. Thus, the crack could be idealised by a two-DOF system, including the crack depth denoted as 'a' and the half-length denoted as 'c'. As depicted in Fig. 2, the notation of DOFs is followed by a subscript 'tc' or 'rc', which respectively stands for the toe crack and root crack.

In simulating the FCG process, the Paris model [29] is employed to predict the increase in crack sizes with cycles, as shown in Eq. (1).

$$\frac{da}{dN} = C\bullet(\Delta K_a(N))^m, \frac{dc}{dN} = C\bullet(\Delta K_c(N))^m \tag{1}$$

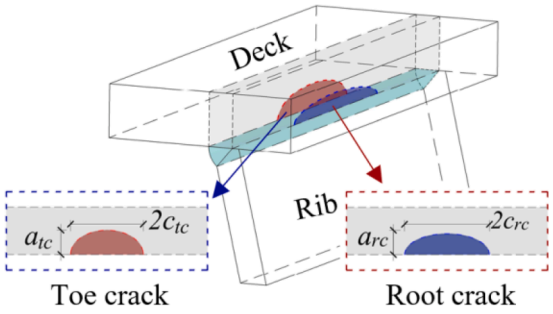

Fig. 2. Crack model of the RD joint.

where a and c represent the crack depth and half-length, respectively; N is the number of loading cycles; C and m are the crack growth rate and power index, respectively; ΔK_a and ΔK_c are the range of SIFs at the crack tip and edge, which is varied with N.

Based on Eq. (1), the crack size at an arbitrary time t can be estimated with applied loading cycles through integration, as shown in Eq. (2).

$$a_t = \int_0^{N_t} (C\bullet(\Delta K_a(N))^m)dN \tag{2a}$$

$$c_t = \int_0^{N_t} (C\bullet(\Delta K_c(N))^m)dN \tag{2b}$$

where a_t and c_t are the crack depth and half-length; N_t is the number of loading cycles at time t.

Since the explicit solution of SIFs is unavailable in most cases, Eq. (2) is usually approximated by a series of fracture analysis at discrete time points, in which the crack size is gradually increasing step-by-step [44]. For enough accuracy, the increment in crack size should be limited to a reasonable value, e.g., 1% of the current crack size.

2.2. Probabilistic modelling of fracture parameters

Probabilistic modelling is carried out on the parameters in the proposed FCG model to consider the uncertainty in the initial flaw size and crack growth rule, as shown in Fig. 3. The initial flaw size is modelled by the flaw depth and the aspect ratio, through which the correlation between the depth and half-length of the flaw is implicitly simulated [45]. Several datasets of the initial flaw size could be found from the literature [46]-[49], which were derived from the non-destructive test. The above datasets were measured from ships or offshore structures, differing from the configuration of OSDs. Meanwhile, the tested specimens were fabricated in the 1970 s-1990 s, which may not reflect the state-of-the-art advance in welding technologies. However, as a practical issue, a comprehensive dataset could be hardly found on the initial flaw size of RD joints in OSDs.

Hopefully, this study mainly aims at the influence of mixed failure models rather than the accurate estimation of fatigue life. The early age measurement may not reflect the recent technical development but could result in a more conservative prediction. Besides, the cruciform and tee butt welded joints in [46]-[49] are highly similarly to the RD joint in terms of the detailed configuration. Moreover, the initial flaw in the noted cruciform and tee butt joints also shows the semi-elliptical shape, which is the same as assumed in the crack model in Fig. 2. Among the literature [46]-[49], the dataset reported from [4849] is the most comprehensive one. To this end, the initial flaw depth and aspect ratio are derived using the data from [4849], as shown in Fig. 3a and b.

In terms of the Paris law, the crack growth rate is modelled as a random variable, and the power index is set as a deterministic value of 3.0 as suggested by [32]. The distribution of the crack growth rate is reproduced via the mean and design value in [50], as shown in Fig. 3c.

The critical crack size is introduced to identify the final state of the single cracking model, i.e., failure occurs once the critical size is ach-

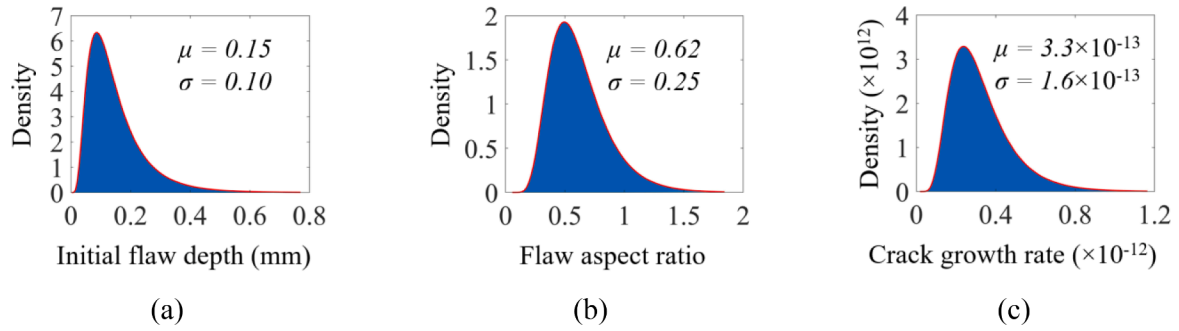

Fig. 3. Distribution of variables in the PFCG model: (a) Initial flaw depth [4849]; (b) Aspect ratio of the initial flaw [4849]; (c) Crack growth rate [50].

ieved in either crack depth or length direction. In the case of crack depth, the critical size a_f is set as the thickness of the deck plate. In terms of the critical half-length, a notably larger value of $c_f = 200mm$ is assumed, above which the safety and serviceability of OSDs would be seriously impacted [4]. The weld toe is usually completed with a welding quality inferior to that of the weld root due to the sudden arc blow-out and spatter [51], variation in the flank angle [52] and potential under-cut [53] at the toe. To this end, two cases are considered in this study: (1) Case I - the distribution of initial flaw depth and aspect ratio is the same at the root and toe; (2) Case II - the mean and standard deviation of initial flaw depth at the toe are two times the values at the root while the aspect ratio is the same.

2.3. Limit state function and reliability block diagram

As aforementioned, this study marks the failure of the sole cracking model by the achievement of the critical crack size in either crack depth or length. Thus, the limit state function (LSF) of a sole cracking model (i.e., TTD or RTD) can be written as Eq. (3).

$$G\left(\dot{X}_i, t\right) = \left(a_i(t) - a_f\right) \cup \left(c_i(t) - c_f\right), \forall i = tc \ \ or \ \ rc \tag{3}$$

where $\dot{X}_i$ is the state vector of the type i cracking model.

Accordingly, the probability of failure (PF) of a sole cracking model can be derived as Eq. (4).

$$P_{f,i} = P\left[G\left(\dot{X}_i, t\right) \le 0\right] = 1 - \left(1 - P_{f,a_i}\right) \bullet \left(1 - \mathrm{P}_{\mathrm{f},c_i}\right), \quad \forall \mathrm{i} = \mathrm{tc} \ \ \mathrm{or} \ \ \mathrm{rc} \tag{4}$$

where $P_{f,i}$ is the PF of the *ith* cracking model; P_{f,a_i} and P_{f,c_i} stand for the achievement of the critical crack size at the depth and length, respectively.

Meanwhile, the failure of the RD joint is assumed once any of the two cracking models occur. To this end, the failure of the RD joint could be idealised as a two-level hierarchical series system, as shown by the reliability block diagram (RBD) in Fig. 4.

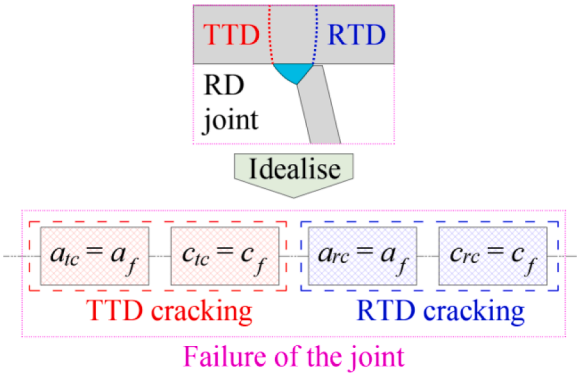

Fig. 4. System-level RBD of the RD joint.

Accordingly, the system-level PF of the RD joint can be predicted using Eq. (5).

$$P_{f,RD} = 1 - \left(\left(1 - P_{f,a_{tc}}\right) \bullet \left(1 - \mathrm{P}_{\mathrm{f},c_{tc}}\right)\right) \bullet \left(\left(1 - \mathrm{P}_{\mathrm{f},a_{rc}}\right) \bullet \left(1 - \mathrm{P}_{\mathrm{f},c_{tc}}\right)\right) \tag{5}$$

where $P_{f,RD}$ is the system-level PF of the RD joint; $P_{f,a_{tc}}$ and $P_{f,c_{tc}}$ are respectively the probability of the achievement of the critical size in depth and length under the TTD cracking; $P_{f,a_{rc}}$ and $P_{f,c_{tc}}$ respectively standard for the achievement of the critical size in depth and length under the RTD cracking.

The MCS is then employed to solve Eq. (4) via sampling, as shown in Eq. (6).

$$P_{f,RD} = \frac{\sum_{i=1}^{n_{MCS}} I\left[\left(a_{tc} \ge a_f \cup c_t \ge c_f\right) \cup \left(a_{rc} \ge a_f \cup c_r \ge c_f\right)\right]_i}{n_{MCS}} \tag{6}$$

Where n_{MCS} is the sample size of MCS; $I[\ ]_i$ is the true-or-false indicator by the *ith* sample.

3. Random traffic-based derivation of stress spectra

3.1. Selected prototype bridge

A typical OSD bridge in Chengdu, China, is selected as the prototype to derive the vehicle-induced stress spectra in RD joints, as shown in Fig. 5. The bridge has a span of 50,000 mm, which is simply supported by the fixed hinge on one end and the slide hinge on another end. Along the span, the OSD of the bridge is divided into 14 segments by the floor beams spaced at 3,500 mm.

The 12,500 mm-wide OSD carries three lanes with different functions, including one fast lane, one middle land and one slow lane. Within the three lanes, a total of 15 U-ribs are distributed with 30 RD joints.

Since the fatigue-critical lorries are likely to run in the slow lane, the RD joint close to the left footprint of the centrally loaded vehicle is chosen as the joint of interest.

3.2. Random traffic model

The random traffic model proposed in [54] is applied to incorporate the uncertainty in vehicle loads, as shown in Fig. 6.

Overall, the vehicles have been grouped into six types with different occupancy rate in the slow lane, according to the configuration and axle weight. It is worth stating that the model excludes lightweight passenger cars because of their little contribution to fatigue damage [55]. Two kinds of axles are assumed for each vehicle type, including the steering axle marked in blue and the rear axle marked in red. Accordingly, two types of footprints are assumed, i.e., 300 × 200 mm (width and length) for the steering axle with single-tire and 600 × 200 mm for the rear axle with dual-tire.

Apart from the vehicle configuration, the axle weight of each vehicle type is also modelled as random variables. As per the feature of the axle weight, the Gaussian mixed model (GMM) is employed to fit the distribution, which could have multiple peaks. Fig. 7 shows the probability

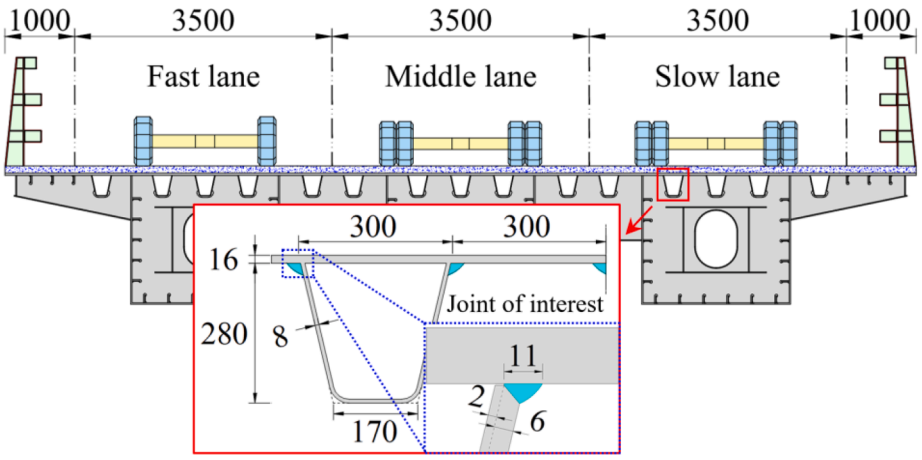

Fig. 5. Selected prototype bridge and the RD joint of interest (Unit: mm).

Type	Vehicle configuration (m)	Occupancy rate in slow lane (%)
V1	2.89	45.5
V2	5.26 1.89	1.69
V3	1.89 5.07	2.82
V4	1.88 4.54 1.34	4.34
V5	3.53 6.58 1.31 1.31	6.15
V6	3.17 1.41 6.58 1.31 1.31	39.5

Fig. 6. The vehicle types and occupancy rate of the used random traffic model [54].

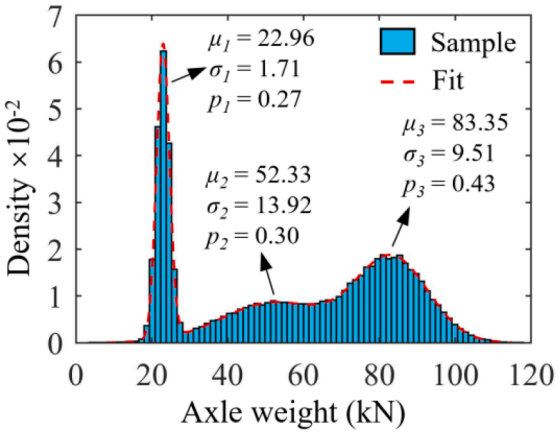

Fig. 7. Weight distribution of the 3rd axle in the type V5 vehicle.

density of the weight of the 3rd axle in the type V5 vehicle, and the details about other axles can be found in [40].

Meanwhile, the lateral distribution of the vehicle centre is considered according to EC1 [33], as shown in Fig. 8. For the convenience of numerical implementation, the original discrete distribution is fitted

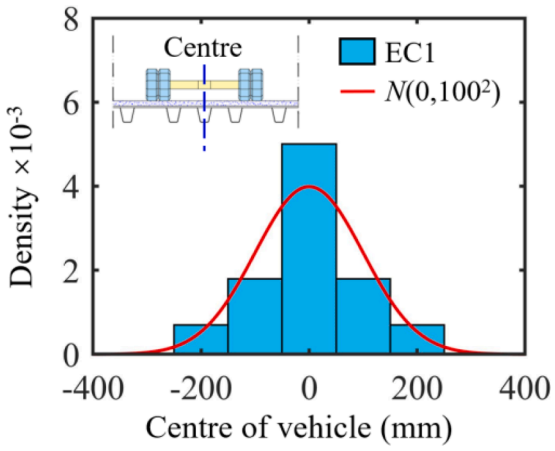

Fig. 8. Lateral distribution of vehicle centre.

into the continuous Gaussian distribution. Based on the above model, the vehicles are generated through conditional sampling due to the interdependence among the variables in the random traffic model, as shown in Fig. 9.

The vehicle type and lateral position are at first sampled. Then, the sample size of each vehicle type is determined after its proportion and the total sample size of MCS. Conditioned on the vehicle type, sampling is made for the number of axles, axle space, and axle weight. The number of axles and axle space are two deterministic values directly associated with the vehicle type, as shown in Fig. 6. Meanwhile, the axle weight is sampled using the edge distribution conditioned on the vehicle type, as

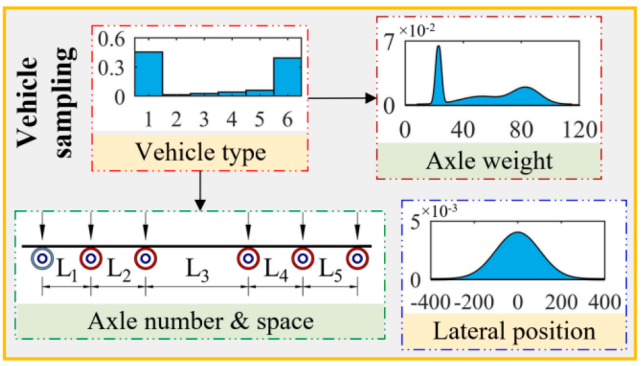

Fig. 9. Conditional sampling of vehicles.

shown in Eq. (7).

$$P(W_i) = \sum_{j=1}^{6} P(V_j)P(W_i|V_j) \tag{7}$$

where W_i is the weight of the *ith* axle; V_j stands the *jth* vehicle type.

The traffic volume is described by the average daily traffic (ADT) with the Gaussian distribution, as shown in Fig. 10. The measurement in [54] is used to calculate the mean value of the ADT, while its standard deviation is determined after the COV of 0.2 reproduced from the data in [55].

3.3. Influence surface-based derivation of stress spectra

A multi-scale FE model of the selected bridge is established [56] to derive the vehicle-induced stress spectra, as shown in Fig. 11. For the balance between accuracy and efficiency, the FE model is modelled by three parts with different meshing strategies, including the global model of the bridge, the sub-model of the segment under investigation, and the highly refined model of the interested RD joint.

The global model is meshed with a relatively coarse element size (i.e., 20 mm-wide and 50 mm-long) since it is mainly used to transfer the boundary condition from the global model to the sub-model. Then, the sub-model is discretised using a finer element size of 10 × 10 mm. The global model and sub-model are meshed separately and then coordinated via the multi-point constraint (MPC) algorithm [57]. Meanwhile, the refined model of the interested RD joint is directly embedded into the sub-model by the sharing nodes on the interface. To this end, the adaptive meshing is employed to generate a smooth transition of element size from 10 × 10 mm to 2 × 2 mm at the core region where the stress to be extracted. As suggested by IIW [32], this study leverages the nominal stress on the deck bottom, which is calculated at the point 1.5 times deck thickness (i.e., 24 mm) from the toe or root. Meanwhile, in the length direction, the vehicle-induced stress range is extracted at the centre of the joint, to account for the most critical situation. Meanwhile, the influence surface method [40] is exploited to boost the FE model-based derivation of the stress spectra using the random traffic model. Fig. 12 shows the influence surface solved for the dual-tire of 60 kN.

Based on the influence surface, the stress history of a sampled vehicle could be easily derived by the linear operation. For the illustration purpose, a standard V6 truck is applied to derive the stress history at the weld toe and root, as shown in Fig. 13.

The axle weight of the standard truck is set as the upper quantile of 97.7%, and the truck is assumed to pass through the centre of the slow lane. Obviously, one stress range is generated by each axle. Besides, it is interesting that the stress at the middle surface is almost ignorable compared with the stress at the bottom surface. Thus, only the bending

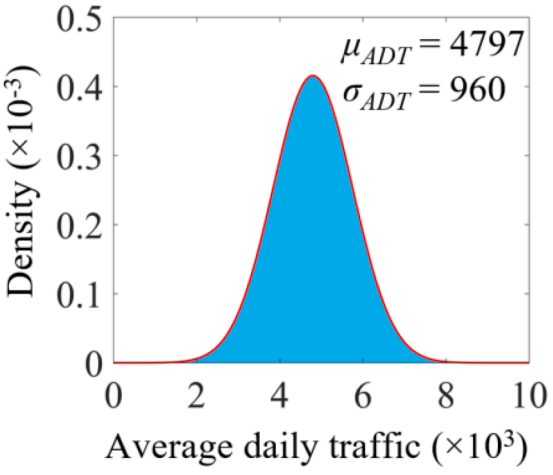

Fig. 10. Distribution of the ADT.

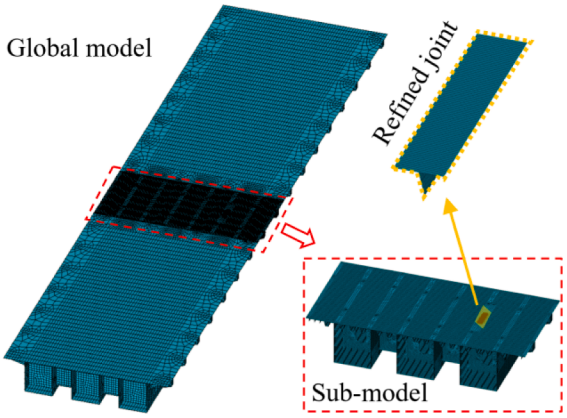

Fig. 11. Multi-scale FE model of steel bridge.

stress is considered in the SIF calculation in the following section.

Based on the above method, a comprehensive database of the stress history is derived through a total of 10^7 MCS. After that, the rain-flow approach [58] is used to transform the stress history into a series of stress ranges and the corresponding number of cycles. Recalling the Paris law in Eq. (1), since the same crack size is assumed in a single solution step, the above stress ranges could be converted into one equivalent stress range, as illustrated in Eq. (8).

$$\Delta\sigma_e = \sqrt[m]{\sum_{i=1}^{n_{sr}} N_i \bullet \sigma_i^m} \tag{8}$$

where $\Delta\sigma_e$ is the equivalent stress range; n_{sr} is the number of stress ranges; σ_i and N_i are the *ith* stress range and the corresponding number of cycles.

Then, the database of equivalent stress range is established and fitted via the GMM model, as shown in Fig. 14. The distribution of the equivalent stress range shows two crests with similar proportions (i.e., 45% vs 55%), including a narrow peak in the lower region and a flat one centred on the upper region. The lightweight steering axle is deduced as the major cause for the crest in the lower region, for which the density enriches to form a narrow peak. On the contrary, the crest in the upper region is induced by the rear axle, of which the diversity in weight leads to the flatness of the crest.

4. Gaussian process regression-assisted solution of SIFs

4.1. Introduction to Gaussian process regression

As aforementioned, the extremely high computational cost hinders the application of FE-based PFCG simulation. This study tries to find an alternative solution by hiring the machine learning tool, Gaussian process regression (GPR) [59], to boost the FE-based PFCG analysis. The GPR is one of the regression-based methods like the commonly used polynomial regression. The major difference between the GPR and the traditional regression method lies in the consideration of the correlation in errors between the prediction and data. In the traditional regression methods, it is assumed the error follow the independent and identical distribution (IID) [60], as shown in Eq. (9).

$$g(\dot{x}) = \xi(\dot{x})^T\dot{\theta} + \dot{\varepsilon} \tag{9}$$

where $g(\dot{x})$ is the total response on the $n_d \times 1$ input vector $\dot{x}$; $\dot{\theta}$ is a $n_p \times 1$ vector defining the parameters in the basis function; $\xi(\dot{x})$ stands for the explicit basis function to transform $\dot{x}$ from $\mathbb{R}^{n_d}$ to $\mathbb{R}^{n_p}$ space; $\dot{\varepsilon}$ is the $n_d \times 1$ vector of errors, which follows the zero mean IID with the unbiased variance.

Alternatively, the error is assumed to be inter-correlated in the GPR. Accordingly, the error is simulated by latent variables following the

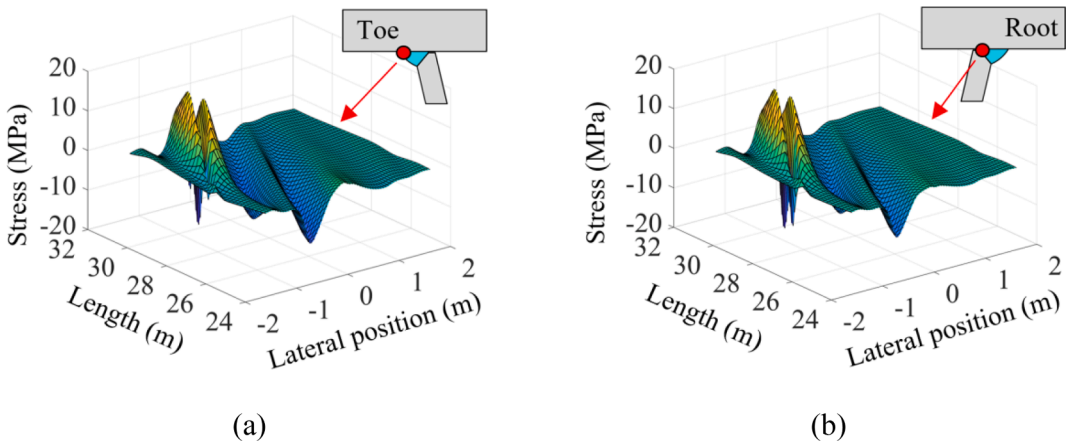

Fig. 12. Influence surface of nominal stress under the dual tire of 60 kN: (a) Weld toe; (b) Weld root.

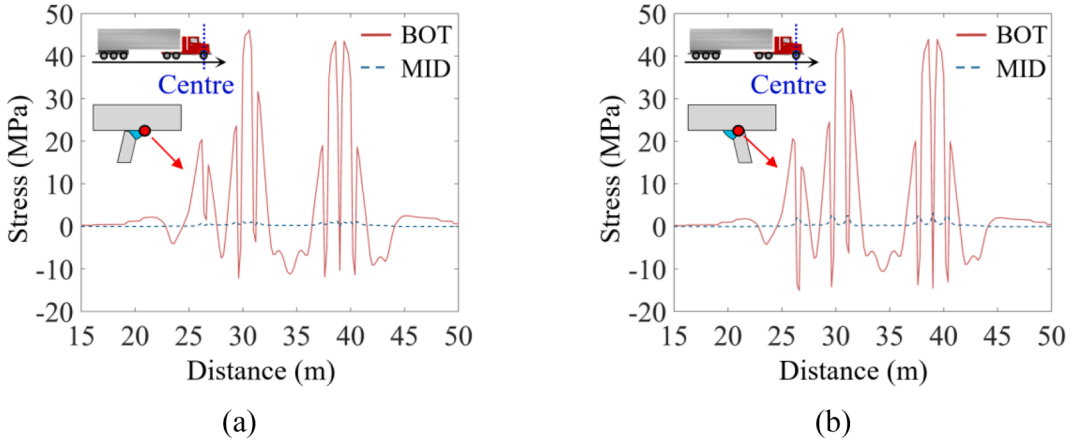

Fig. 13. Stress history solved with the standard V6 truck: (a) Weld toe; (b) Weld root.

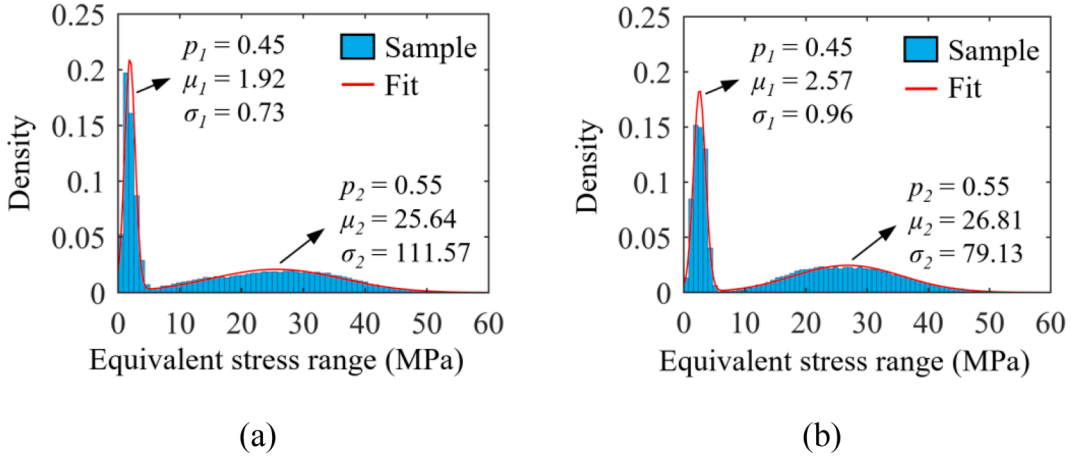

Fig. 14. Stress spectra derived by random traffic model: (a) Weld toe; (b) Weld root.

zero-mean Gaussian process, as shown in Eq. (10).

$$g(\dot{x}) = \xi(\dot{x})^T\dot{\theta} + f(\dot{x}) \tag{10a}$$

$$f(\dot{x}) \sim GP(0, r(\dot{x}, \dot{x}^{'})) \tag{10b}$$

where $f(\dot{x})$ is the $n_d \times 1$ vector of latent variables; $r(\dot{x}, \dot{x}^{'})$ is the covariance function.

Unlike the traditional regression, the GPR is nonparametric due to the introduction of latent variables. The prediction depends on the training data rather than the basis function. The distribution of the predicted response at the new input could be expressed in a Bayesian way, as shown in Eq. (11).

$$P\left(y_p|\dot{y}_t, \boldsymbol{X}_t, \dot{x}_p\right) = N\left(\xi\left(\dot{x}_p\right)^T\dot{\theta} + \mu, \sigma^2 + \Sigma\right) \tag{11a}$$

$$\mu = r\left(\dot{x}_p, \boldsymbol{X}_t\right)\left(r(\boldsymbol{X}_t, \boldsymbol{X}_t) + \sigma^2 I\right)^{-1}\left(\dot{y}_t - \xi\left(\dot{x}_t\right)^T\dot{\theta}\right) \tag{11b}$$

$$\Sigma = \mathrm{r}\left(\dot{x}_p, \dot{x}_p\right) - r\left(\dot{x}_p, \boldsymbol{X}_t\right)^T\left(r(\boldsymbol{X}_t, \boldsymbol{X}_t) + \sigma^2 I\right)^{-1} r\left(\dot{x}_p, \boldsymbol{X}_t\right) \tag{11c}$$

where y_p is the predicted response; $\dot{x}_p$ is the $n_d \times 1$ vector of the new input; $\boldsymbol{X}_t$ is the $n_t \times n_d$ matrix of training inputs, in which n_t is the number of train samples; y_t is the $n_t \times 1$ vector of training responses; σ is the nature noise; I is the $n_t \times n_t$ identity matrix.

On this basis, the expectation of the prediction could be expressed as shown in Eq. (12).

$$\overline{y}_p = \xi\left(\dot{x}_p\right)^T\dot{\theta} + r\left(\dot{x}_p, \boldsymbol{X}_t\right)\left(r(\boldsymbol{X}_t, \boldsymbol{X}_t) + \sigma_n^2 I\right)^{-1}\left(\dot{y}_t - \xi\left(\dot{x}_t\right)^T\dot{\theta}\right) \tag{12}$$

The covariance function could be defined by various types of kernel functions conditional on the kernel parameter vector $\dot{\beta}$, i.e., $r\left(\dot{x}, \dot{x}^{'}|\dot{\beta}\right)$. Meanwhile, the parameters $\dot{\theta}$, $\dot{\beta}$ and σ could be estimated from the training data via maximizing the likelihood $P\left(\dot{y}_t|\boldsymbol{X}_t\right)$, as shown in Eq. (13).

$$\widehat{\dot{\theta}}, \widehat{\dot{\beta}}, \widehat{\sigma} = \underset{\dot{\theta},\dot{\beta},\sigma}{\mathrm{argmax}}\log P\left(\dot{y}_t\middle|\boldsymbol{X}_t, \dot{\theta}, \dot{\beta}, \sigma\right) \tag{13}$$

where $\widehat{\dot{\theta}}, \widehat{\dot{\beta}}, \widehat{\sigma}$ are respectively the estimator of $\dot{\theta}, \dot{\beta}, \sigma$.

The GPR has been extensively applied in solving Engineering issues. Especially, the GPR is highly similar or even equivalent to the classical Kriging interpolation [61] in Geostatistics, except for a very subtle difference in their mathematical form. Meanwhile, several preliminary applications of the GPR could also be found in the fatigue evaluation. Zhu et al. [62] employed the FE-trained GPR model as an alternative to the influence surface method in deriving the vehicle-induced stress in OSDs. Hu et al. [63] used the GPR to surrogate the FE model in simulating the fatigue crack growth of turbine disks, through the computational efficiency is notably improved.

Apart from the GPR, the deep neural network (DNN) is also a promising machine learning tool for the above regression task. Especially, the DNN becomes now very popular due to its power in handling massive data. However, the performance of the DNN is usually controlled by the selection of hyperparameters, including the learning rate, number of epochs, network structure, batch size, etc. As aforementioned, the GPR is a nonparametric method, in which the practical issue associated with the selection of hyperparameters could be effectively ameliorated. Meanwhile, it is very interesting that, the DNN with infinite width has been proved to be equivalent to the GPR in their mathematic nature [64]. Besides the above benefits, the GPR performs inadequately in handling massive data. Due to the matrix inversion involved, as shown in Eqs. (11) and (12), the GPR has a computational complexity of $O(N^3)$ [65]. As a result, the GPR is prone to be numerically intractable with the amount of training data. Another issue is the tendency of overfitting by the GPR when nature noise is remarkable in the training data. Hopefully, the training data in this study are generated by FE simulations, of which the uncertainty is very limited. Meanwhile, the amount of train data is relatively moderate. Due to the above two features of train data, the GPR could be feasible and efficient enough to handle the data in this study.

4.2. Feature selection

A crucial step before the application of the above GPR is the preparation of training data. As illustrated in Eq. (1), a key issue in simulating the crack growth is to calculate the range of SIFs under vehicle loads. In the previous Section 3, the stress spectra of the interested RD joint have been already derived using the random traffic model, as shown in Fig. 14a and b. Thus, the calculation of vehicle induced-SIF ranges could be converted into the assignment to solve SIF ranges under various stress ranges. The stress range-induced alternation in SIFs could be expressed by the general form shown in Eq. (14).

$$\Delta K_i = Y_i \Delta\sigma\sqrt{\pi a}, \quad \forall i = a \ \ or \ \ c \tag{14}$$

Where ΔK_i is the range of SIFs at the crack tip or edge; Y_i stands for the correction factor at the crack tip or edge, which depends on the detail geometry and crack shape; $\Delta\sigma$ is the applied stress range; a is the crack depth.

As suggested by Eq. (14), for the same crack shape in the same detail, the SIF range is in proportion to the stress range. Meanwhile, the configuration of the RD joint in this study is assumed as the same. Besides, this study employs the semi-elliptical crack model with two DOFs at the crack tip and edge, as shown in Fig. 2. Based on the above three conditions, the calculation of SIF ranges could be further simplified into the solution of the unit stress-induced SIF under different combinations of crack depth and half-length, as shown in Eq. (15).

$$\overline{K}_i = Y_i(a, c)\sqrt{\pi a}, \quad \forall i = a \ \ or \ \ c \tag{15}$$

where $\overline{K}_i$ is the SIF solved under unit stress, called as the unitised SIF for abbreviation; a and c are the crack depth and half-length, respectively.

In order to consider the interaction between the toe crack and root crack, the predicting SIF is assumed to depend on the size of both two cracks. In another word, all the four crack size parameters are selected as the training feature while the SIF is selected as the training label, as shown in Eqs. (16a) and (16b).

$$\overline{K}_{i,t} = \overline{K}_{i,t}(a_t, c_t, a_r, c_r), \quad \forall i = a \ \ or \ \ c \tag{16a}$$

$$\overline{K}_{i,r} = \overline{K}_{i,r}(a_t, c_t, a_r, c_r), \quad \forall i = a \ \ or \ \ c \tag{16b}$$

where $\overline{K}_{i,t}$ and $\overline{K}_{i,r}$ stand for the SIF solved for the toe crack and root crack, respectively.

In the case when only one crack is considered, the above interaction is ignored, and Eq. (16) could be simplified into the prediction using two variables, as shown in Eqs. (17a) and (17b).

$$\overline{K}_{i,t} = \overline{K}_{i,t}(a_t, c_t), \quad \forall i = a \ \ or \ \ c \tag{17a}$$

$$\overline{K}_{i,r} = \overline{K}_{i,r}(a_r, c_r), \quad \forall i = a \ \ or \ \ c \tag{17b}$$

4.3. Data preparation and training

In preparing the train data for the GPR, a local FE model of the RD joint is established using ANSYS [56], as shown in Fig. 15a. The model is 59 mm wide to ensure that the remote stress range is loaded at the exact point of the nominal stress defined in Section 3.3 (i.e., 24 mm from the point to the crack toe or root). At the same time, the remote stress range is assumed constant along the cracked region [44], by which the complexity of the local model is reduced in a conservative way. To this end, the local FE model only covers the possible length of the cracked region to save the computational cost. As result, the length of the local model is determined as 500 mm to contain the maximum crack length of $2c_f = 2 \times 200mm$ (see Section 2.2). Meanwhile, as aforementioned in Section 3.3, only the bending stress is focused on, due to the little contribution of membrane stress in the total stress. Based on the above, the local model is applied with the same boundary condition along the length, i.e., loaded by unit bending stress at the left and right while fixed at the bottom edge. Meanwhile, no constraint is placed on the front and rear edges of the model to approximate the quasi-plane stress state for the cracked region.

The multi-scale modelling strategy is also applied, for which the local model and the highly refined crack body are meshed separately. Then, the crack body is connected with the local model via the surface-to-

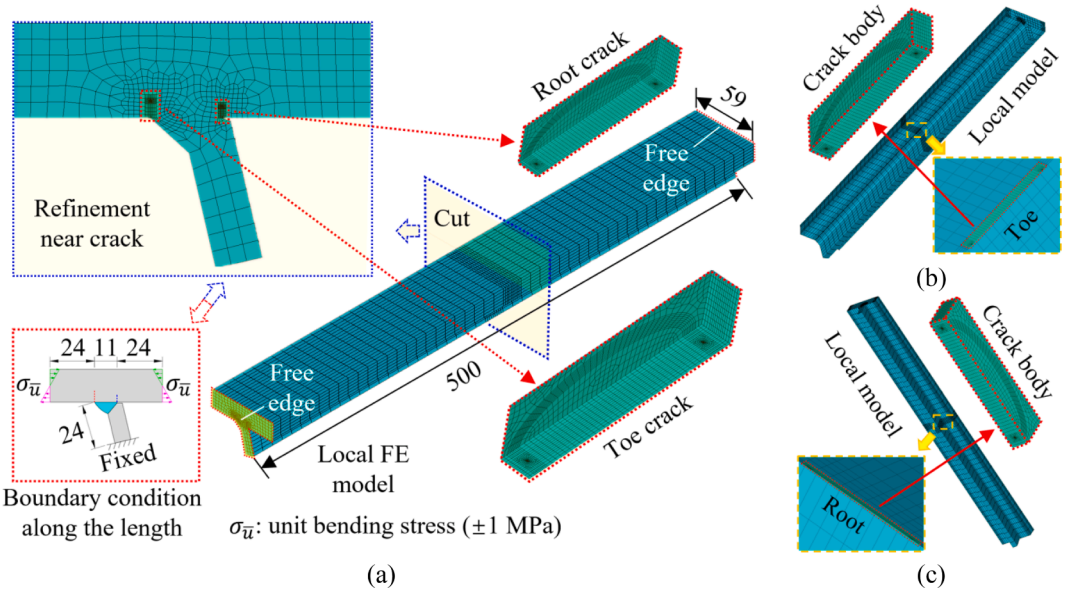

Fig. 15. Local FE model of cracked RD joints: (a) Dual-cracks; (b) Toe crack; (c) Root crack.

surface contact [57]. The toe crack and root crack have been modelled at the same time, in order to consider the interaction between the two cracks. In solving SIFs, the interaction integral method [66] has been applied, with a total of 6 contours requested. For the numerical stability, the result is determined by averaging from the 2nd to 6th contours [57].

For better comparison, the same method and boundary condition have been employed to establish the local FE model containing the solo-crack, i.e., toe crack or root crack, as shown in Fig. 15b and c. The configuration of the solo-crack model has also been kept the same as that in the dual-cracks model. By employing the above FE models, training data have been generated by sampling, including 2,000 samples for the dual-cracks model, and 500 samples for each of the solo-crack models. The samples are selected through Latino hypercube sampling (LHS) [67] with the repeated point eliminated, which ensure the even distribution of training data.

To avoid lengthy illustration, the following only shows the validation of the trained GPR for the dual-crack model in detail. The trained GPR of the dual-crack model is visualised by the blue grid in Figs. 16 and 17, accompanied by the independent test data plotted in red markers. The test data are also sampled by the above LHS method, but the SIF is solved by the local FE model instead of the GPR. For better illustration, the GPR is plotted for the toe crack and root crack one by one, in which the parallel crack beside the concerned one is fixed at a small size of 0.15 mm-deep and 0.48 mm-long. Intuitively, the result suggests a very good agreement between the FE solution and the GPR prediction, indicating the accuracy and feasibility of the trained GPR model.

For the comparison in a quantitative way, the mean squared error (MSE) has been also calculated between the test data and GPR prediction, as shown in Eq. (17).

$$MSE = \frac{1}{N}\sum_{i=1}^{N}(y_i - \hat{y}_i)^2 \tag{17}$$

where y_i and $\hat{y}_i$ are the ith testing and predicted outputs; N is the amount of testing data.

The MSE calculated from the additional FE result is included in Figs. 16 and 17. Obviously, the small value of MSEs shows a good performance of the trained GPR model in surrogating the FE simulation. Moreover, the influence of parallel crack size has also been investigated, as shown in Fig. 18a and b. Four different levels of the parallel crack sizes have been considered, including 25%, 50%, 75% and 100% of the concerned crack size. As a result, the influence of the parallel crack is not apparent when its size is relatively small compared with the concerned crack. As the parallel crack becomes comparable to the concerned one, the influence becomes obvious but still moderate.

Further validation of the GPR is also carried out within the training data. Firstly, the 5-folds cross-validation [68] has been employed, which

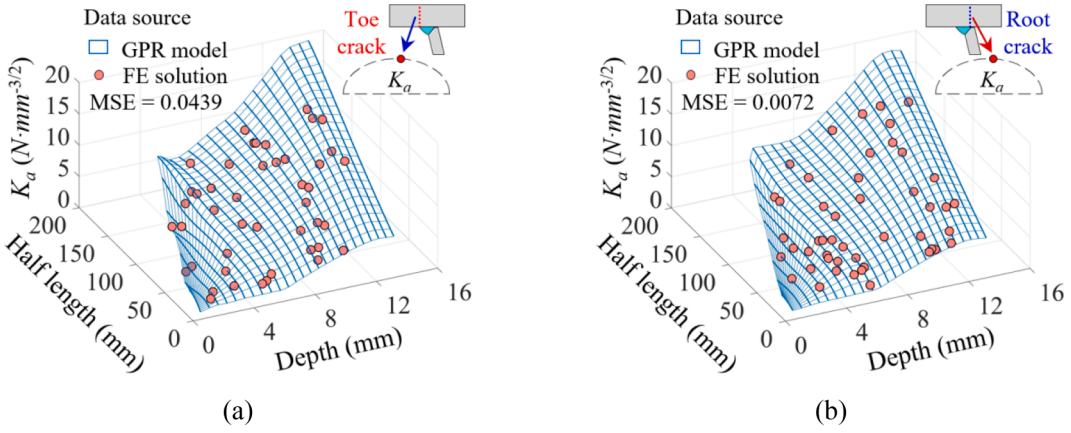

Fig. 16. GPR-predicted SIF at the crack tip with the fixed parallel crack: (a) Weld toe; (b) Weld root.

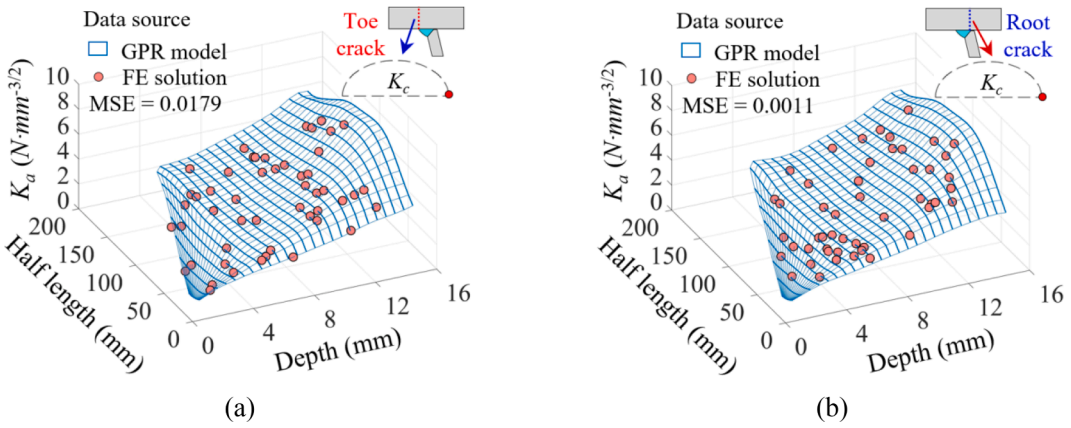

Fig. 17. GPR-predicted SIF at the crack edge with the fixed parallel crack: (a) Weld toe; (b) Weld root.

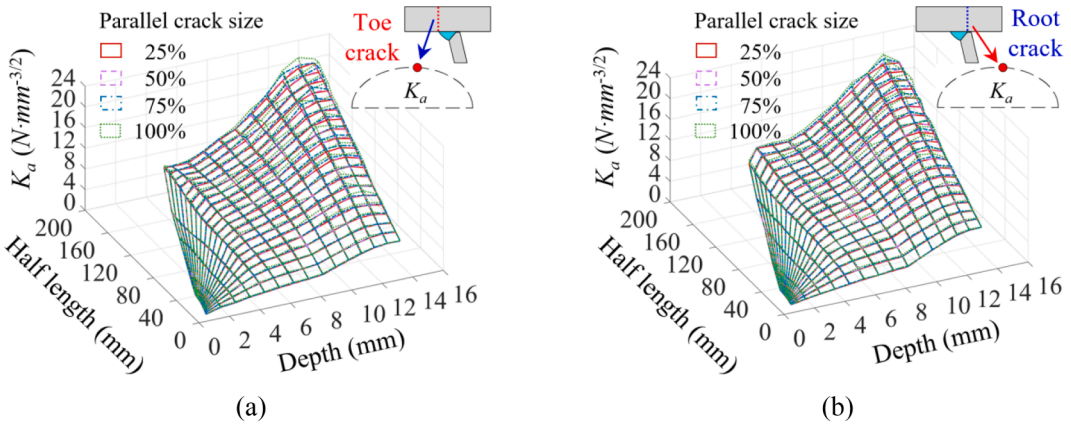

Fig. 18. GPR-predicted SIF at the crack tip with different parallel cracks: (a) Weld toe; (b) Weld root.

is commonly applied to test the accuracy and robustness of data-driven models. During the cross-validation, the training data are divided into 5 approximately equal blocks. The validation will run 5 times, accordingly. In the *i*th of 5 runs, the *i*th block will be used as the testing data, and the other 4 blocks will sever as the training data. Then, the GPR model will be trained by the 4 blocks and tested against the *i*th block. Due to the copious amount of training data, the MSE is also employed to show the result of the cross-validation in a concise way, as listed in Table 1. It is worth noting that, the MSE from the cross-validation is even lower than from the test data by the FE solution. Meanwhile, the goodness-of-fit is also verified for the trained GPR using the adjusted coefficient of multiple determination (also called adjusted R^2) [60], as shown in Eq. (18).

$$\text{adjusted } R^2 = 1 - \frac{N-1}{N-(K+1)} \cdot \frac{\sum_{i=1}^{N}(y_i - \hat{y}_i)^2}{\sum_{i=1}^{N}(y_i - \bar{y})^2} \tag{18}$$

where $\bar{y}$ is the mean of testing outputs; K is the number of variables, which set as 4 in this study.

The results are also summarized in Table 1. The adjusted-R^2 is approaching the upper limit of 1, indicating a strong goodness-of-fit that most of the training data could be explained by the GPR model. Based on the above investigation, the GPR model is validated to surrogate the FE model in solving SIFs.

4.4. Process of GPR-assisted solution

Fig. 19 shows the whole process of GPR-assisted solution using the PFCG model. At first, random samples are generated based on the established probabilistic models, including the crack growth rate, initial flaw size, average daily truck traffic and equivalent stress range. After that, fatigue crack growth simulation is carried out for each sample in an incremental way until the failure or run-out. In the simulation, the trained and validated GPR model is used to surrogate the FE-based fracture analysis in the SIFs calculation. Compared with the direct FE solution, the computational cost could be greatly reduced through the GPR-assisted simulation. For instance, a total of 20.8 h may be spent to generate a single sample by implementing the FE-based fracture analysis

Table 1
Validation of the trained GPR model.

Crack	location	Symbol	MSE by 5-folds cross-validation						Adjusted-R^2
			Fold-1	Fold-2	Fold-3	Fold-4	Fold-5	Average	
Toe	Tip	K_{at}	0.0004	0.0003	0.0006	0.0004	0.0017	0.0007	0.9998
	Edge	K_{ct}	0.0009	0.0004	0.0005	0.0008	0.0002	0.0006	0.9996
Root	Tip	K_{ar}	0.0001	0.0004	0.0003	0.0001	0.0002	0.0002	0.9995
	Edge	K_{cr}	0.0010	0.0005	0.0003	0.0001	0.0002	0.0004	0.9989

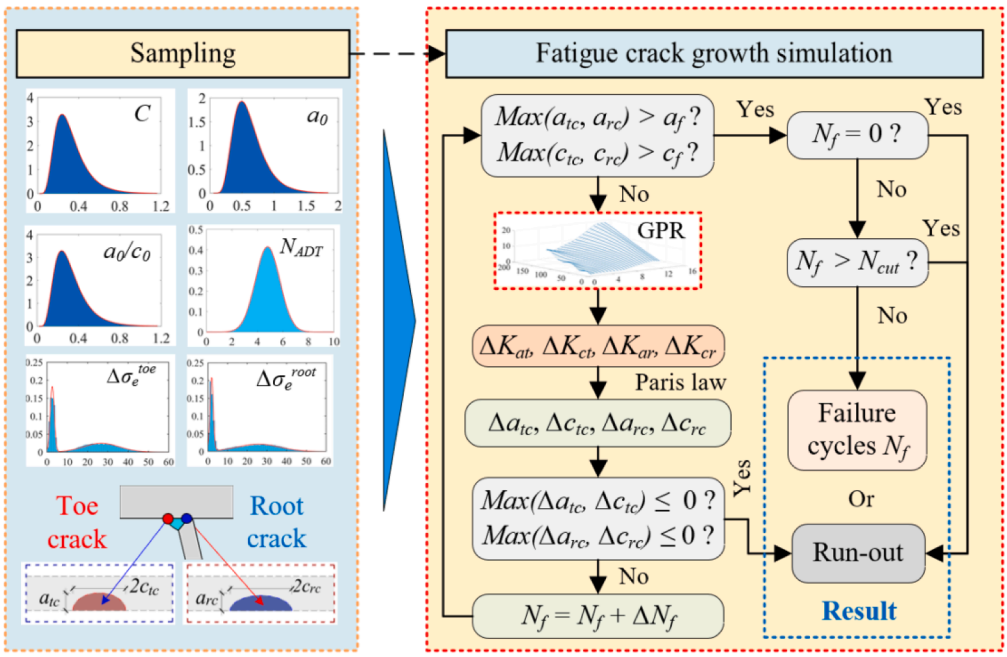

Fig. 19. Flow chart of GPR-assisted solution using the PFCG model.

with a 10-core (Intel i9-10900 K) workstation [68]. Exactly, the efficiency is much higher than the model fatigue test, which usually costs one or two weeks to complete only one specimen. However, the efficiency is still far behind the need for extensive solution efforts imposed by the PFCG analysis.

Alternatively, with the same hardware, the solution time for a single data point using the GPR-assisted approach can be less than 40 s, i.e., more than 1800 times improvement in the computational efficiency. As a result, the flexibility and accuracy of FE-based fracture analysis could be fully incorporated into the PFCG simulation.

5. Result and discussion

5.1. Fatigue failure model

The FCG history of the RD joint could be solved by implementing the PFCG model with the GPR-assisted approach. Fig. 20a and b show the FCG process of two typical failure models solved under the case I and case II (see Section 2.2), respectively. For better illustration, the calculation is carried out in the deterministic way using the mean value. In the case I, the initial flaw size is assumed the same at the weld root and toe. Compared with the toe crack, the root crack shows a slightly higher growth rate and causes the failure of the joint. In the case II, the toe crack replaces the root crack as the failure case. In addition, the final critical crack size of the toe crack is notably larger than that of the root crack in the case II. To sum, the RD joint is prone to the root cracking when the same initial flaw is assumed. However, as a larger initial flaw is assumed at the weld toe in the case II, the toe crack becomes the critical case of the failure.

Apart from the above two failure models, the RD joint also illustrates a third failure model, in which both the toe and root cracks reach the critical size at the same time. However, this both-cracking failure is a

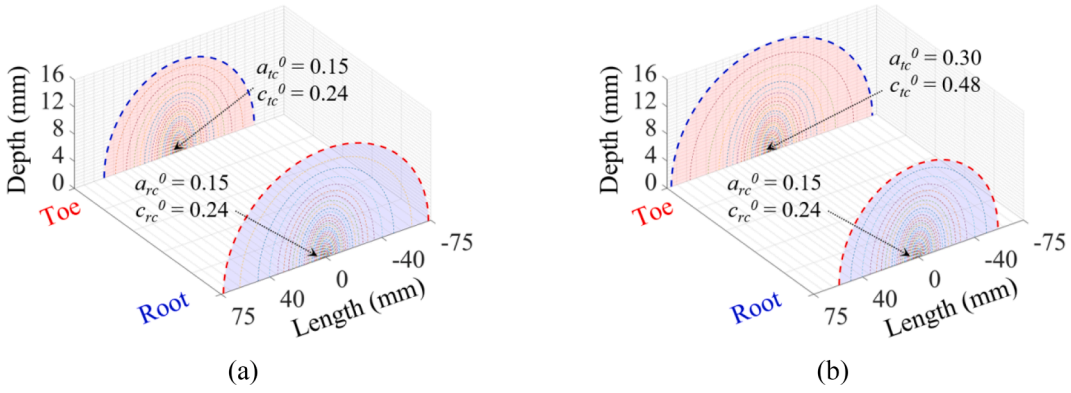

Fig. 20. FCG process of two typical fatigue failure models: (a) Case I; (b) Case II.

coincident event rarely that happens in a sense of statistics. A total of 10^6 MCS are performed to investigate the proportion of the three failure models, as shown in Fig. 21.

In both the cases I and II, the both-cracking failure shows a proportion well below 3.1%, which could be regarded as an event of small probability [60]. In the case I, the probability of the RTD cracking is about 51.0% higher than that of the TTD cracking, i.e., 74.3% vs 23.3%. In the case II, the RD shows an increased tendency of the TTD cracking about 13.3% higher than that in the RTD cracking. Generally, both the TTD cracking and RTD cracking contributes to the fatigue failure notably. However, this effect would be overlooked if only the governing failure model is employed to assess the fatigue performance. Meanwhile, from a statistical point of view, the dominance of failure models depends on the initial flaw size, which represents the welding quality.

5.2. Fatigue reliability and life prediction

Further investigation is made on the fatigue reliability and life prediction of the interested RD joint (see Fig. 5). For better comparison, the reliability is also estimated using the PSN approach proposed in [40], with the same fatigue strength assumed for the TTD cracking and RTD cracking. A total of 10^7 MCS are conducted for the service life from 20 to 120 years, as shown by the time-variant reliability curve in Fig. 22. Since the OSD is a highly redundant system, its fatigue cracking is more likely an issue of serviceability [69]. According to JCSS [70], three reliability levels (i.e., 1.3, 1.7 and 2.3) are introduced for the comparison and life prediction, which are denoted as the lower, middle, and upper safety lines.

In the case I, the reliability solved by the PFCG is slightly higher than the result by the PSN at the very beginning. With the increase in service life, the PFCG result crosses through the PSN result after about 25 years and decreases at a much higher rate. In terms of the PFCG, the systematic reliability crosses the above three safety lines after about 67, 87, and 104 years, respectively, which stands for the life prediction under the three criteria. On the contrary, the corresponding reliability curve of the PSN decreases below the upper line after roughly 110 years and is well above the other two lines after 120 years. This can be traced back to the nonlinear fatigue damage accumulation in the PFCG model since the SIF increases proportionally with the crack size. As a result, the PSN approach may lead to an overestimated life since the nonlinear damage accumulation is ignored.

The result also shows slightly lower reliability of the RTD in the case I, compared with the TTD cracking. Moreover, the system-level reliability is even lower than that of the RTD, indicating the importance of mixed failure models. For instance, by taking $\beta = 1.3$ as the bottom line, the fatigue life could be estimated as about 120 years when considering the RTD only. Once the influence of mixed failure models is considered in the system-level reliability, a much shorter life would be resulted as about 100 years. Similar trends can be observed in the result solved under the case II, while the reliability of the TTD cracking becomes a slightly lower than that of the RTD cracking. However, the PSN result stays the same as in the case I since the change in the initial flaw size is not explicitly modelled in the PSN approach.

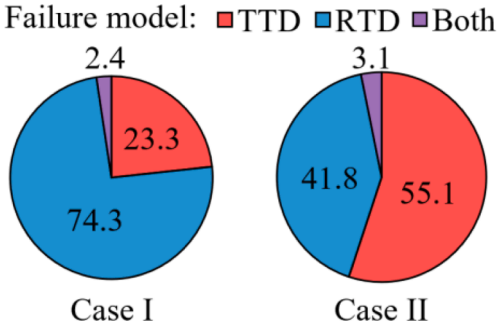

Fig. 21. Proportion of different failure patterns.

Apart from the reliability index, the investigation has been also carried out on the evolution in the distribution of the remain fatigue life after a certain period of exploitation, as shown in Fig. 23. It is worth stating that the remain life has no upper limit in theory since the continuous distribution is employed in the PFCG modelling. However, the remain life in Fig. 22 is truncated at 1,000 years, above which the probability is lower than 0.1% and has no practical mean.

With the time increasing, the entire distribution moves leftward, and the probability density gradually accumulates around zero. As a result, the distribution changes from the original lognormal shape to the normal form at $t = 40$ years, and then to the gamma distribution at $t = 80$ years, and finally to almost the exponential one at the end of $t = 120$ years. It is worth noting that, the probability density skyrockets after 120 years, even if the expectation of remain life is 163.19 years in case 1 and 158.91 years in case 2. Thus, it is revealed by the evolution in the distribution shape that the RD joint deteriorates at an increasing rate.

5.3. Crack size evolution

In addition to the fatigue reliability and life prediction, another crucial feature of the PFCG model is the ability to model the variation in crack size explicitly. Thus, the investigation is performed on the time-dependent evolution of the crack size, as shown in Fig. 24.

A total of 4 time points is selected, including the 30, 60, 90, and 120 years. For better illustration, the distribution of crack half-length is truncated at a cut-off of 40 mm, above which the probability density drops to an ignorable value. According to the result, both the mean value and standard deviation of the crack size increase over the service time. As a result, the distribution of crack sizes moves right and transforms from a narrow curve into a flat one. Meanwhile, the distribution density accumulates at the critical crack depth of 16 mm over time, indicating progressive growth in the failure probability. However, the distribution still stays in the almost lognormal form once eliminating the concertation at the critical size. The comparison is made on the size distribution between the toe and root cracks. In general, the mean value of both the crack depth and length are slightly larger in the root crack than in the toe crack. However, an opposite trend could be found in the standard deviation, of which the toe crack has a higher value than the root crack.

In addition, the study also examines the time-dependent variation in the aspect ratio of crack length to depth, as shown by the boxplot in Fig. 25. In both root and toe cracks, the data dispersion decreases from the initial peak value to its trough at 60 years and slowly escalates until 120 years.

However, the dispersion at the end of 120 years is still much lower than the initial one. Meanwhile, the aspect ratio distribution also demonstrates a progressive evolution of skewness, i.e., from the initial positive skewness to the normal curve at 40 years and then to the negative skewness at 120 years.

6. Conclusions

In this study, a probabilistic fatigue crack growth (PFCG) model is established for the rib-to-deck (RD) joint considering mixed failure models. Based on the observation reported in the literature, two typical failure models are incorporated in the PFCG model, including the toe-to-deck (TTD) cracking and root-to-deck (RTD) cracking. In implementing the PFCG model, the Gaussian process regression (GPR) is used to assist and boost the fracture analysis after well trained and validated. Using the above approach, a series of investigations are carried out on the RD joint respecting the fatigue failure model, fatigue reliability and life prediction, crack size evolution, and remain fatigue life. Above all, the following conclusions are drawn.

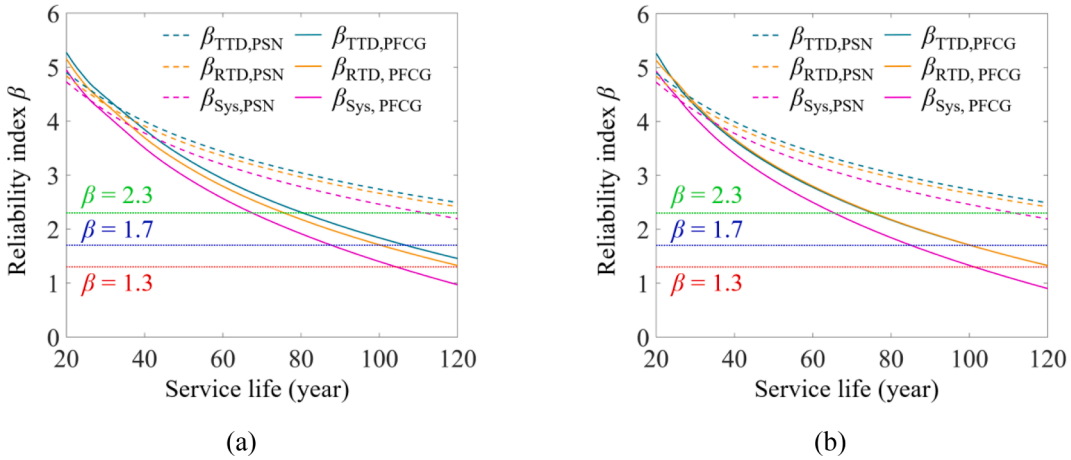

Fig. 22. Time-variant fatigue reliability: (a) Case I; (b) Case II.

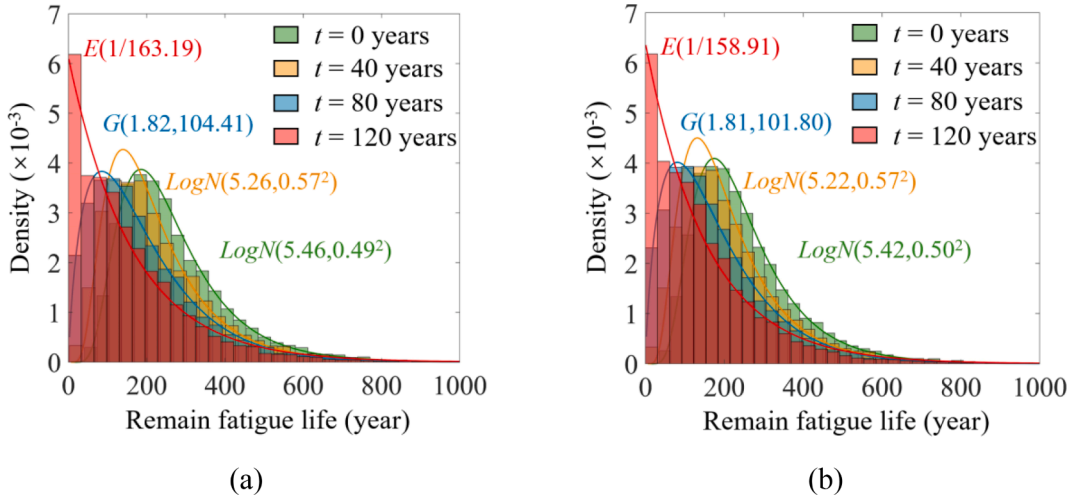

Fig. 23. Distribution of remain fatigue life at $t = 0$, 40, 80 and 120 years: (a) Case I; (b) Case II.

(1) Through the application of the GPR in assisting the PFCG simulation, the computational efficiency improves more than 1800 times compared with the pure FE solution. As a result, the PFCG simulation could be implemented with a delicate balance between accuracy, efficiency, and flexibility.

(2) Besides the TTD and RTD cracking models, the RD joint shows a third cracking model with a very small possibility no more than 3.1%, i.e., the TTD cracking and RTD cracking occur simultaneously. In the case I that the same initial flaw is assumed, the RD joint is more prone to the RTD cracking (74.3%) than the TTD cracking (23.3%). In the case II that the assumed flaw size is doubled at the weld toe due to the inferior welding quality, the TTD cracking (55.1%) replace the RTD cracking (41.8%) as the dominant one. In both cases, the secondary cracking model shows a notable contribution to fatigue failure in a statistical sense, indicating the importance in considering mixed failure models.

(3) The reliability of the RTD cracking is slightly lower than that of the TTD cracking in the case I, which also indicates the inclination to the RTD cracking. Moreover, the system-level reliability considering mixed failure models is even lower than the RTD cracking. As result, the fatigue life would be overestimated using the dominant cracking model only. For instance, taking $\beta = 1.3$ as the bottom line, the fatigue life is close to 120 years under the RTD cracking, compared with a shorten life of roughly 100 years in the system-level reliability.

(4) The remain fatigue life after a certain period of exploitation shows a notable transformation in the distribution shape, i.e., from the original lognormal shape to the normal form at 40 years, and to the gamma shape at 80 years, and then to the exponential one at 120 years. As a result, the probability density rapidly enriches in the lower region, which in turn escalates the failure probability quickly even with a notable mean value.

(5) The distribution of crack size shows a steady development in both the mean value and standard deviation, while it stays in almost the lognormal form. As a result, the probability density function gradually moves right and transforms from a narrow curve on the left to a flat one. In terms of the aspect ratio, the dispersity decreases rapidly at the first and then escalates slowly over time. Besides, the distribution of the aspect ratio also shows a progressive evolvement from original positive skewness to the normal form after 40 years, and then to the negative skewness at the end of 120 years.

In general, this study highlights the influence of mixed failure models on rib-to-deck (RD) welded joints in steel bridge decks by establishing and implementing a probabilistic fatigue crack growth (PFCG) model, with the help of the machine learning tool, Gaussian process regression (GPR). However, the physical part of the PFCG model is simplified since the study mainly aims at the influence of mixed failure models. Future efforts are expected to treat the fatigue crack growth and associated

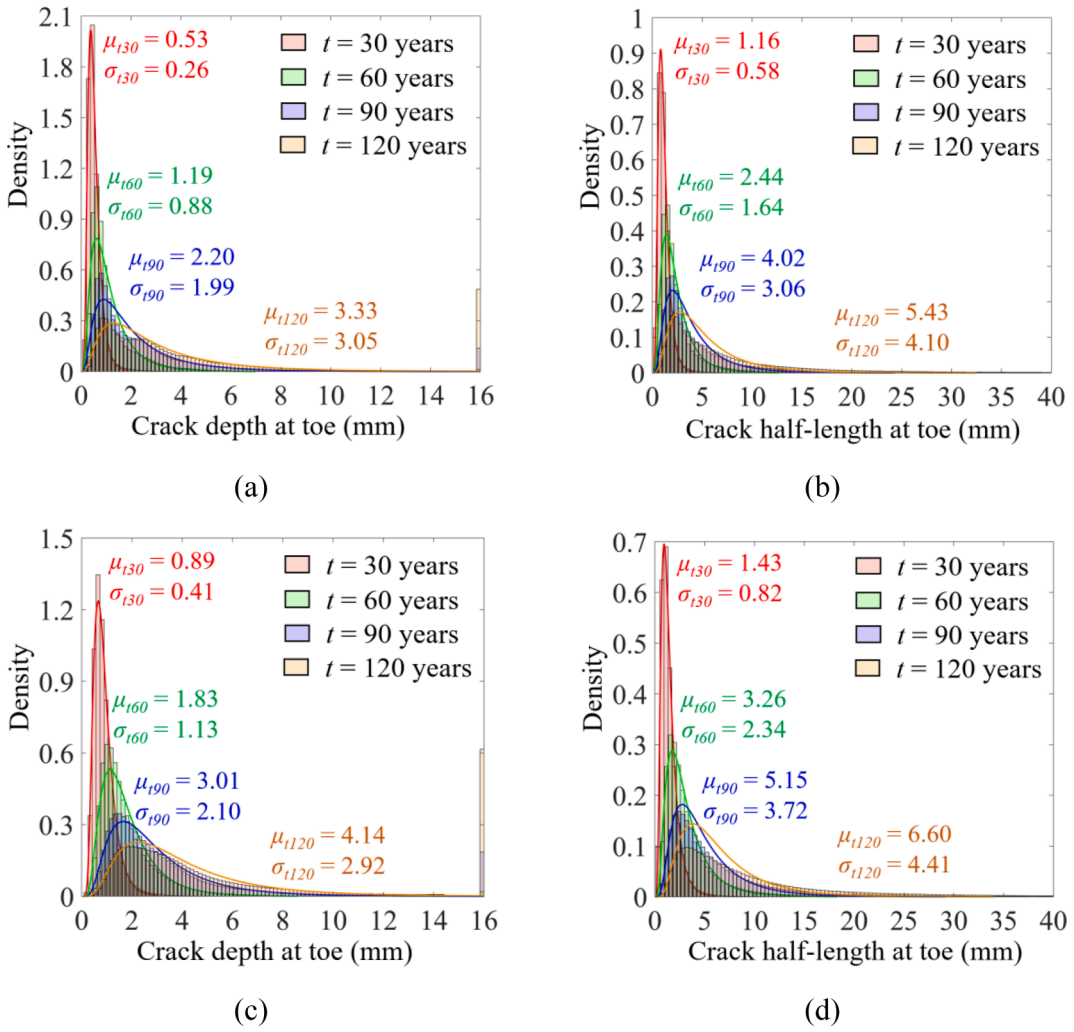

Fig. 24. Crack size distribution at $t = 30$, 60 and 120 years: (a) crack depth at toe; (b) crack half-length at toe; (c) crack depth at root; (d) crack half-length at root.

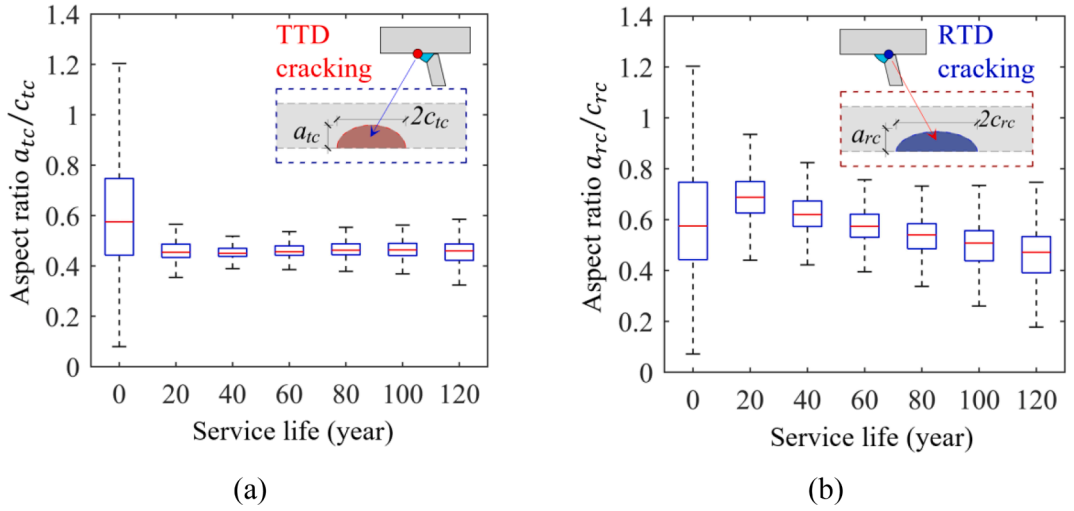

Fig. 25. Evolution of aspect ratio: (a) Weld toe; (b) Weld root.

uncertainties in a more detailed way. Firstly, the actual length of the RD joint could be modelled to simulate the crack growth with the stress intensity factors (SIFs) directly, instead of using the equivalent stress range to solve SIFs. Secondly, the uncertainty could be considered in the local geometries of RD joints since it is a major source of deviation in fatigue performance, e.g. the plate thickness, weld flank angle, weld leg length, lack of penetration rate, etc. Finally, it could be considered in the PFCG model that the random cracks initiate and coalesce from multiple

initial flaws along the RD joint, by which the influence of joint length could be revealed.

CRediT authorship contribution statement

Junlin Heng: Methodology, Investigation, Data curation, Writing – original draft. **Zhixiang Zhou:** Conceptualization, Supervision, Funding acquisition. **Yang Zou:** Formal analysis, Validation, Writing – review & editing. **Sakdirat Kaewunruen:** Writing – review & editing.

Declaration of Competing Interest

The authors declare that they have no known competing financial interests or personal relationships that could have appeared to influence the work reported in this paper.

Acknowledgement

The study is supported by the National Natural Science Foundation of China (grant number: 51778536, 52008066) and Shenzhen Key Laboratory of Structure Safety and Health Monitoring of Marine Infrastructures (grand number: ZDSYS20201020162400001).

Date Availability Statement

Some or all the data, model or code employed in this paper are available from TU Delft repository after the essential embargo as well as available from the corresponding author upon reasonable request.

References

[1] Kozy BM, Connor RJ, Paterson D, Mertz DR. Proposed Revisions to AASHTO-LRFD Bridge Design Specifications for Orthotropic Steel Deck Bridges. J Bridge Eng 2011; 16(6):759–67. https://doi.org/10.1061/(ASCE)BE.1943-5592.0000214.
[2] Connor R, Fisher J, Gatti W, et al. Manual for design, construction, and maintenance of orthotropic steel deck bridges. Washington, DC, US: Federal Highway Administration; 2012.
[3] Dooren F., Nagtegaal G., Ashurst D., Gration D., Blanken S., ander & Kunst, Pajc. (2010). Orthotropic Deck Fatigue: Renovation of 8 Bridges in the Netherlands. Structural Faults and Repair-2010: 13th International Conference. https://doi.org/10.13140/RG.2.1.1571.1200.
[4] Kolstein MH. Fatigue Classification of Welded Joints in Orthotropic Steel Bridge Decks. Delft, the Netherlands: Gildeprint Drukkerijen B.V.; 2007.
[5] Wu M, Zhu J, Heng J, Kaewunruen S. Fatigue Assessment on Suspenders under Stochastic Wind and Traffic Loads Based on In-Situ Monitoring Data. Appl Sci 2019;9(16):3405. https://doi.org/10.3390/app9163405.
[6] Steel Construction Committee of JSCE. Survey and research report by the subcommittee of plate welded joints. Tokyo, Japan: JSCE Publications; 2007 (In Japanese).
[7] Heng, J., Zheng, K., Zhang, Y., Wang, Y. (2018). Enhancing fatigue performance of rib-to-deck joints in orthotropic steel decks using thickened edge U-ribs. In: ASCE Struct. Cong. 2018, Reston, VA., US.
[8] Tian Y, Li Y, Zhang D, Dai Y. Static and fatigue test research on welded rib-to-deck connections in steel orthotropic steel bridge deck. J Rail Sci Eng 2011;8(2):34–9 (In Chinese).
[9] Heng J, Zheng K, Gou C, Zhang Y, Bao Y. Fatigue performance of rib-to-deck joints in orthotropic steel decks with thickened edge u-ribs. J Bridge Eng 2017;22(9): 04017059. https://doi.org/10.1061/(asce)be.1943-5592.0001095.
[10] Heng J, Zheng K, Kaewunruen S, Zhu J, Baniotopoulos C. Probabilistic fatigue assessment of rib-to-deck joints using thickened edge U-ribs. Steel Compos Struct 2020;2:23–56.
[11] Cheng Bin, Ye Xinghan, Cao Xinger, Mbako Dibu Dave, Cao Yishan. Experimental study on fatigue failure of rib-to-deck welded connections in orthotropic steel bridge decks. Int J Fatigue 2017;103:157–67.
[12] Nagy Wim, Wang Benjin, Culek Bohumil, Van Bogaert Philippe, De Backer Hans. Development of a fatigue experiment for the stiffener-to-deck plate connection in Orthotropic Steel Decks. Int J Steel Struct 2017;17(4):1353–64. https://doi.org/10.1007/s13296-017-1207-8.
[13] Li M, Suzuki Y, Hashimoto K, Sugiura K. Experimental Study on Fatigue Resistance of Rib-to-Deck Joint in Orthotropic Steel Bridge Deck. J Bridge Eng 2018;23(2): 04017128. https://doi.org/10.1061/(ASCE)BE.1943-5592.0001175.
[14] Ocel J, Cross B, Wright W, Yuan H. Optimization of rib-to-deck welds for steel orthotropic bridge decks. Washington, DC, US: Federal Highway Administration; 2017.
[15] Yamada K, Ya S. Plate bending fatigue tests for root crack of trough rib of orthotropic steel deck. JSCE J Struct Eng 2008;54:675–84.
[16] Ya S, Yamada K, Ishikawa T. Fatigue evaluation of rib-to-deck welded joints of orthotropic steel bridge deck. J Bridge Eng 2010;16(4):492–9.
[17] Lv P, Li D. Fatigue test study on the rib-to-deck welded joint in orthotropic steel decks. J Zhengzhou Univ (Eng Sci) 2013;34(2):89–93 (In Chinese).
[18] Fu Z, Ji B, Zhang C, Wang Q. Fatigue performance of roof and U-rib weld of orthotropic steel bridge deck with different penetration rates. J Bridge Eng 2017;22 (6):04017016.
[19] Sim H, Uang C, Sikorsky C. Effects of Fabrication Procedures on Fatigue Resistance of Welded Joints in Steel Orthotropic Decks, Journal of Bridge Engineering. J Bridge Eng 2009;14(5):366–73. https://doi.org/10.1061/(ASCE)1084-0702(2009)14:5(366).
[20] Kainuma S, Yang M, Jeong Y, Inokuchi S, Kawabata A, Uchida D. Experiment on fatigue behavior of rib-to-deck weld root in orthotropic steel decks. J Constr Steel Res 2016;119:113–22. https://doi.org/10.1016/j.jcsr.2015.11.014.
[21] Wang C, Zhai M, Tang Y, Chen W, Qu T. Numerical Fracture Mechanical Simulation of Fatigue Crack Coupled Propagation Mechanism for Steel Bridge Deck. China J Highway & Transport 2017;30(3):82–95 (In Chinese).
[22] Li J, Zhang Q, Bao Y, Zhu J, Chen L, Bu Y. An equivalent structural stress-based fatigue evaluation framework for rib- to-deck welded joints in orthotropic steel deck. Eng Struct 2019:196. https://doi.org/10.1016/j.engstruct.2019.109304.
[23] Luo P, Zhang Q, Bao Y, Zhou A. Fatigue evaluation of rib-to-deck welded joint using averaged strain energy density method. Eng Struct 2018;177:682–94. https://doi.org/10.1016/j.engstruct.2018.09.090.
[24] European committee for standardization (CEN). EN 1993: Eurocode 3 - design of steel structures. Brussels, Belgium: CEN; 2005.
[25] Ministry of communications of the People's Republic of China. Specifications for design of highway steel bridges (GB/T D64–2015). Beijing, China: CCPress; 2015 (in Chinese).
[26] AASHTO, AASHTO LRFD bridge design specifications, 9th edition. Washington, DC., US., 2020.
[27] Shen C. The statistical analysis of fatigue data. PhD Thesis. Tucson: University of Arizona; 1994.
[28] Huang Zuwei, Lei Junqing, Guo Shulun, Tu Jian. Fatigue performance of U-rib butt welds in orthotropic steel decks. Eng Struct 2020;211:110485. https://doi.org/10.1016/j.engstruct.2020.110485.
[29] Anderson TL. Fracture Mechanics: Fundamentals and Applications. Fourth Ed. Baca Raton, FL, US: CRC Press; 2017.
[30] Berg N, Xin H, Veljkovic M. Effects of residual stresses on fatigue crack propagation of an orthotropic steel bridge deck. Mater Design 2020;198(2021):109294. https://doi.org/10.1016/j.matdes.2020.109294.
[31] Biondini F, Frangopol D. Life-Cycle Performance of Deteriorating Structural Systems under Uncertainty: Review. J Struct Eng 2016;142:F4016001. https://doi.org/10.1061/(ASCE)ST.1943-541X.0001544.
[32] Hobbacher A. Recommendations for Fatigue Design of Welded Joints and Components. Basel, Switzerland: Springer; 2016.
[33] European committee for standardization. EN 1991: Eurocode 1 - Actions on structures - part 2: traffic loads on bridges. Brussels, Belgium: CEN; 2003.
[34] Kwon K, Frangopol D. Bridge fatigue reliability assessment using probability density functions of equivalent stress range based on field monitoring data. Int J Fatigue 2010;32:1221–32.
[35] Heng J, Zheng K, Kaewunruen S, Baniotopoulos C. Stochastic Traffic-Based Fatigue Life Assessment of Rib-to-Deck Welding Joints in Orthotropic Steel Decks with Thickened Edge U-Ribs. Appl Sci 2019;9(13):2582. https://doi.org/10.3390/app9132582.
[36] Zhu J, Zhang W. Probabilistic fatigue damage assessment of coastal slender bridges under coupled dynamic loads. Eng Struct 2018;166:274–85. https://doi.org/10.1016/j.engstruct.2018.03.073.
[37] Liu Y, Mahadevan S. Probabilistic fatigue life prediction using an equivalent initial flaw size distribution. Int J Fatigue 2009;31(3):476–87. https://doi.org/10.1016/j.ijfatigue.2008.06.005.
[38] Righiniotis TD, Chryssanthopoulos MK. Probabilistic fatigue analysis under constant amplitude loading. J Constr Steel Res 2003;59(7):867–86.
[39] Guo T, Frangopol D, Chen Y. Fatigue reliability assessment of steel bridge details integrating weigh-in-motion data and probabilistic finite element analysis. Comput Struct 2012;112–113(4):245–57. https://doi.org/10.1016/j.compstruc.2012.09.002.
[40] Heng J, Zheng K, Kaewunruen S, Zhu J, Baniotopoulos C. Dynamic Bayesian network-based system-level evaluation on fatigue reliability of orthotropic steel decks. Eng Fail Anal 2019;105:1212–28. https://doi.org/10.1016/j.engfailanal.2019.06.092.
[41] Maljaars J, Vrouwenvelder A. Probabilistic fatigue life updating accounting for inspections of multiple critical locations. Int J Fatigue 2014;68:24–37.
[42] Maljaars J, Bonet E, Pijpers R. Fatigue resistance of the deck plate in steel orthotropic deck structures. Eng Fract Mech 2018;201:214–28. https://doi.org/10.1016/j.engfracmech.2018.06.014.
[43] Wang B, Zhou X, Backer H, Chen A, Schmidt F. Macro-crack initiation life for orthotropic steel decks considering weld heterogeneity and random traffic loading. Struct Infrastruct Eng 2017;13(12):1639–52. https://doi.org/10.1080/15732479.2017.1315733.
[44] Gupta RS, Xin H, Veljkovic M. Fatigue crack propagation simulation of orthotropic bridge deck based on extended finite element method. Procedia Struct Integrity 2019;22:283–90. https://doi.org/10.1016/j.prostr.2020.01.036.
[45] Amirafshari P, Barltrop N, Wright M, Kolios A. Weld defect frequency, size statistics and probabilistic models for ship structures. Int J Fatigue 2021;145: 106069. https://doi.org/10.1016/j.ijfatigue.2020.106069.

[46] Moan T, Vårdal OT, Hellevig N-C, Skjoldli K. In-service observations of cracks in North Sea jackets. A study on initial crack depth and POD values. In: In: Proceedings of the international conference on offshore mechanics and arctic engineering; 1997. p. 189–98.
[48] Kountouris IS, Baker MJ. Defect assessment: analysis of the dimensions of defects detected by ultrasonic inspection in an offshore structure, CESLIC Report OR8. London, UK: Imperial College of Science and Technology; 1989.
[49] Kountouris IS, Baker MJ. Defect assessment: analysis of the dimensions of defects detected by magnetic particle inspection in an offshore structure. Imperial College Sci Technol Eng Struct 1989. Laboratories.
[50] British Standards Institution (BSI). BS 7910:2015 Guide to methods for assessing the acceptability of flaws in metallic structures. London, UK: BSI Standards Limited; 2015.
[51] Schork B, Kucharczyk P, Madia M, Zerbst U, Hensel J, Bernhard J, et al. The effect of the local and global weld geometry as well as material defects on crack initiation and fatigue strength. Eng Fract Mech 2018;198:103–22. https://doi.org/10.1016/j.engfracmech.2017.07.001.
[52] Zerbst U, Ainsworth RA, Beier HTh, Pisarski H, Zhang ZL, Nikbin K, et al. Review on fracture and crack propagation in weldments - A fracture mechanics perspective. Eng Fract Mech 2014;132:200–76. https://doi.org/10.1016/j.engfracmech.2014.05.012.
[53] Bell R, Vosikovsky O, Bain S. The Significance of Weld Toe Undercuts in the Fatigue of Steel Plate T-Joints. Int J Fatigue 1989;11(1):3–11. https://doi.org/10.1016/0142-1123(89)90041-8.
[54] Guo T, Liu Z, Zhu JS. Fatigue reliability assessment of orthotropic steel bridge decks based on probabilistic multi-scale finite element analysis. Adv Steel Constr 2015;11:334–46. https://doi.org/10.18057/IJASC.2015.11.3.7.
[55] Lu Naiwei, Liu Yang, Deng Yang. Fatigue Reliability Evaluation of Orthotropic Steel Bridge Decks Based on Site-Specific Weigh-in-Motion Measurements. Int J Steel Struct 2019;19(1):181–92. https://doi.org/10.1007/s13296-018-0109-8.
[56] ANSYS. Engineering Simulation and 3D Design Software; ANSYS Inc., Canonsburg, US. http://www.ansys.com/.
[57] ANSYS. Mechanical APDL Documentation. Canonsburg, PA, US: ANSYS Inc.; 2020.
[58] Amzallag C, Gerey JP, Robert JL, Bahuaud J. Standardization of the rainflow counting method for fatigue analysis. Int J Fatigue 1994;16(4):287–93. https://doi.org/10.1016/0142-1123(94)90343-3.
[59] Rasmussen CE, Nickisch H. Gaussian processes for machine learning (GPML) toolbox. The J Machine Learning Res 2010;11:3011–5.
[60] Devore JL. Probability and statistics for engineering and the sciences. Boston: Cengage learning; 2011. https://doi.org/10.2307/2532427.
[61] Cressie N. The origins of kriging. Math Geol 1990;22(3):239–52. https://doi.org/10.1007/BF00889887.
[62] Zhu J, Zhang W, Li X. Fatigue Damage Assessment of Orthotropic Steel Deck Using Dynamic Bayesian Networks. Int J Fatigue 2019;118:44–53. https://doi.org/10.1016/j.ijfatigue.2018.08.037.
[63] Hu Dianyin, Su Xiao, Liu Xi, Mao Jianxing, Shan Xiaoming, Wang Rongqiao. Bayesian-based probabilistic fatigue crack growth evaluation combined with machine-learning-assisted GPR. Eng Fract Mech 2020;229:106933. https://doi.org/10.1016/j.engfracmech.2020.106933.
[64] Lee J, Sohl-dickstein J, Pennington J, Novak R, Schoenholz S, Bahri Y. Deep neural networks as gaussian processes. International Conference on Learning Representations, April 30th - May 3rd. Canada: Vancouver; 2018.
[65] Kim NH, An D, Choi JH. Prognostics and health management of engineering systems. Switzerland: Springer International Publishing; 2017. https://doi.org/10.1007/978-3-319-44742-1.
[66] Yu Hongjun, Kuna Meinhard. Interaction integral method for computation of crack parameters K-T –A review. Eng Fract Mech 2021;249:107722. https://doi.org/10.1016/j.engfracmech.2021.107722.
[67] Bucher C. Computational analysis of randomness in structural mechanics: structures and infrastructures book series. London: CRC Press; 2009. https://doi.org/10.1201/9780203876534.
[68] James G, Witten D, Hastie T, Tibshirani R. An introduction to statistical learning. Switzerland: Springer International Publishing; 2021.
[69] Intel. Central processing units; Intel Inc., Santa Clara, CA., US. http://www.intel.com/.
[70] Imam B, Chryssanthopoulos M. A review of metallic bridge failure statistics. Proceedings of the Fifth International IABMAS Conference. 2010.